ADVANCED
SCIENCE NEWS
www.advancedsciencenews.com

NANO MICRO
small

Self-Assembly

Thermo-Driven Evaporation Self-Assembly and Dynamic Analysis of Homocentric Carbon Nanotube Rings

Hu Li, Han Ouyang, Min Yu, Nan Wu, Xinxin Wang, Wen Jiang, Zhuo Liu, Jingjing Tian, Yiming Jin, Hongqin Feng, Yubo Fan,* and Zhou Li*

Nonvolatile solutes contained in a volatile solvent will self-assemble into various well-organized patterns through evaporation on solid substrates in a confined geometry,[1] which has often been referred to as "coffee stains".[2] Convection flow plays an important role in the self-assembly process. This facile technology has attracted great interest because of its low energy consumption and broad applications, such as electronics and sensors.[3] As a novel material, carbon nanotubes (CNTs) have excellent electrical conductivity and mechanical properties.[4] Some research has reported the fabrication of parallel CNT lines and homocentric CNT rings with precast templates.[5] However, it still remains difficult to directly assemble CNT rings with high density and analyze the dynamics of CNTs in the evaporation system.

Herein, focusing on the above-mentioned issues, we ingeniously designed an experiment setup with a hollow cylinder fixed on a solid substrate, which serves as the thermo-driven evaporation self-assembly system (**Figure 1**a). The design with a removable lid will be beneficial for the timely observation and capturing of the dynamic movement trace of multi-walled CNTs (MWCNTs). Plain silicon wafers (Si-SiO$_2$), and a gold film supported by a silicon wafer, polystyrene (PS), or a flexible polyethylene terephthalate (PET) were selected as the substrates for self assembly (Figure 1b). Based on the Si-SiO$_2$ substrate, we fabricated closely packed and scatteredly packed MWCNT rings simultaneously. On the Au-film substrates, we were able to fabricate smooth MWCNT

rings, rings with waviness, and rings with shuttle-like holes simultaneously. We observed the clear dynamic movement trace of MWCNT aggregations by optical microscopy in the convection flow for the first time, which contributed to the analysis of the self-assembly mechanism of the self-assembled MWCNT patterns. The specific distribution of vari-sized MWCNTs in the smooth rings also provided a new method to verify the dimensional homogeneity of MWCNTs at the nanoscale on a Au substrate. Furthermore, this low-cost, manageable method opens up a new avenue for fabricating harmonic oscillators, tissue engineering scaffolds, and ring-like pattern preparation on flexible transparent applications.

The thermo-driven evaporation self-assembly system consisted of a hollow cylinder, a desired substrate and a heating unit. Si-SiO$_2$ and Au with different Hamaker constants were selected as the desired substrates, respectively (planar view in Figure 1a). The Au substrate was supported by a silicon wafer (SiO$_2$-Au), transparent PS plate (PS-Au), or transparent flexible PET (PET-Au), respectively (Figure 1b). The MWCNT dispersion solution formed a concave meniscus under the combined action of the adhesive forces and internal cohesive forces in the cavity. With the evaporation of the deionized (DI) water, a circular opening and circular contact line (CL) formed in the cavity center under the action of the hollow cylinder (2D profile in Figure 1a). As the circular CL receded from the cavity center (inside) to the edge of the hollow cylinder (outside), homocentric MWCNT rings self-assembled from the inside to the outside on the Si-SiO$_2$ and Au substrates. The MWCNT dispersion solution, and the rigid and flexible substrates with MWCNT rings are displayed in Figure 1b.

Initially, Si-SiO$_2$ was selected as the self-assembly substrate. The upper-left inset depicts the formation sequence of MWCNT rings (see **Figure 2**a). Closely packed rings gradually turned into scattered packed rings from the inside to the outside (see Figure 2b). Small-sized MWCNT bundles turned into large-sized MWCNT bundles and bulky aggregated MWCNT particles along the receding direction of the CL.

The height of a single MWCNT ring on the Si-SiO$_2$ substrate can be seen in Figure 2c. The closely packed MWCNT rings showed a neat edge on the Si-SiO$_2$ substrate (see Figure 2e). The closely packed MWCNT ring possessed a rectangular height profile for its edge. In the inset of Figure 2c we fitted a red curve, which matches the rectangular shape of the height profile, on the basis of the jagged black curve. The distance between the top and bottom of the rectangle

H. Li, Z. Liu, Prof. Y. B. Fan
School of Biological Science and Medical Engineering
Beihang University
No. 37 Xueyuan Road, Haidian District
Beijing 100191, P. R. China
E-mail: yubofan@buaa.edu.cn
H. Ouyang, Dr. M. Yu, Dr. X. X. Wang, W. Jiang,
J. J. Tian, Y. M. Jin, Dr. H. Q. Feng, Prof. Z. Li
Beijing Institute of Nanoenergy and Nanosystems
Chinese Academy of Sciences
National Center for Nanoscience and Technology (NCNST)
Beijing 100083, P. R. China
E-mail: zli@binn.cas.cn
Dr. N. Wu
Department of Otolaryngology Head and Neck Surgery
Institute of Otolaryngology
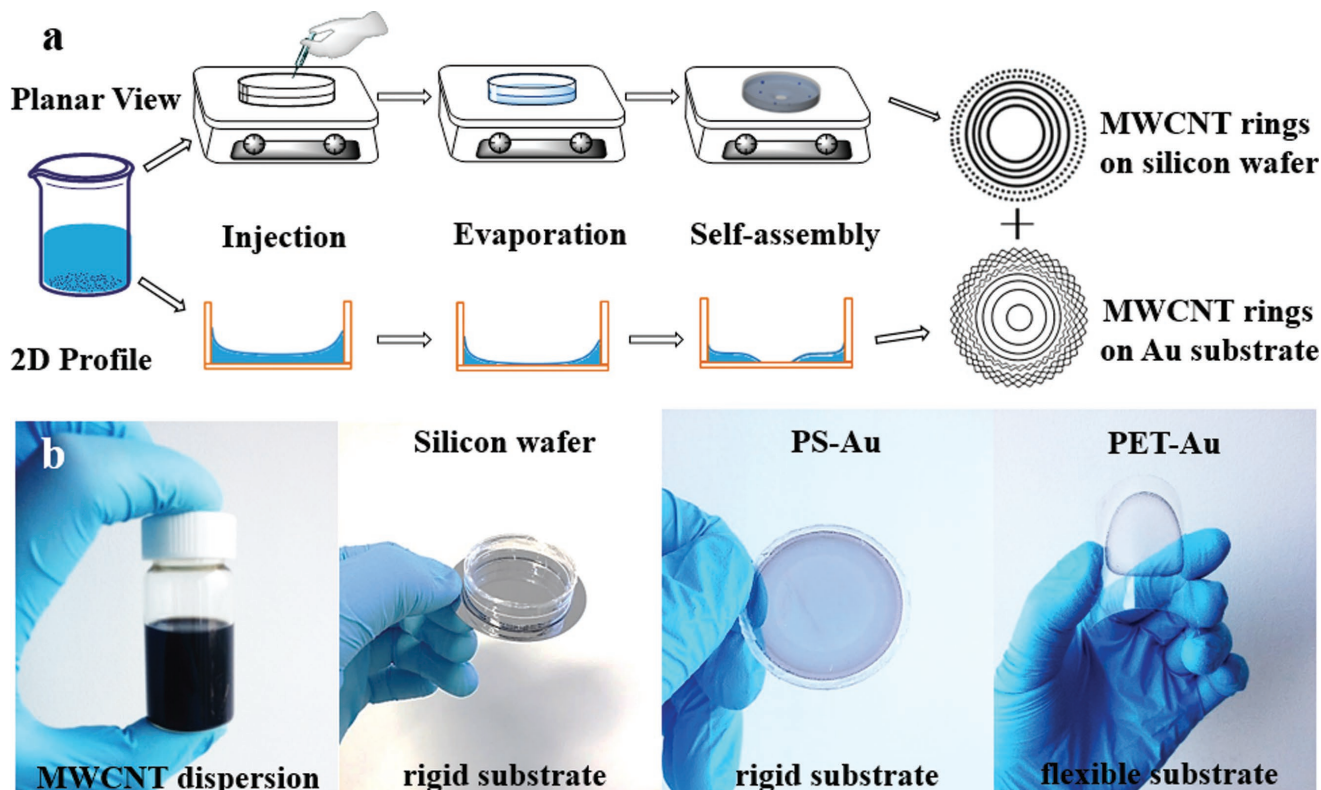Chinese PLA General Hospital
Beijing 100853, P. R. China

Figure 1. Schematic diagram elaborating the self-assembly of various homocentric MWCNT rings. a) The upper side is a planar view of the thermo-driven evaporation self-assembly device. The lower side is a 2D profile depicting the shape evolution of the liquid levels in the cavity. b) Optical photographs of the MWCNT dispersion solution, and the rigid and flexible substrates.
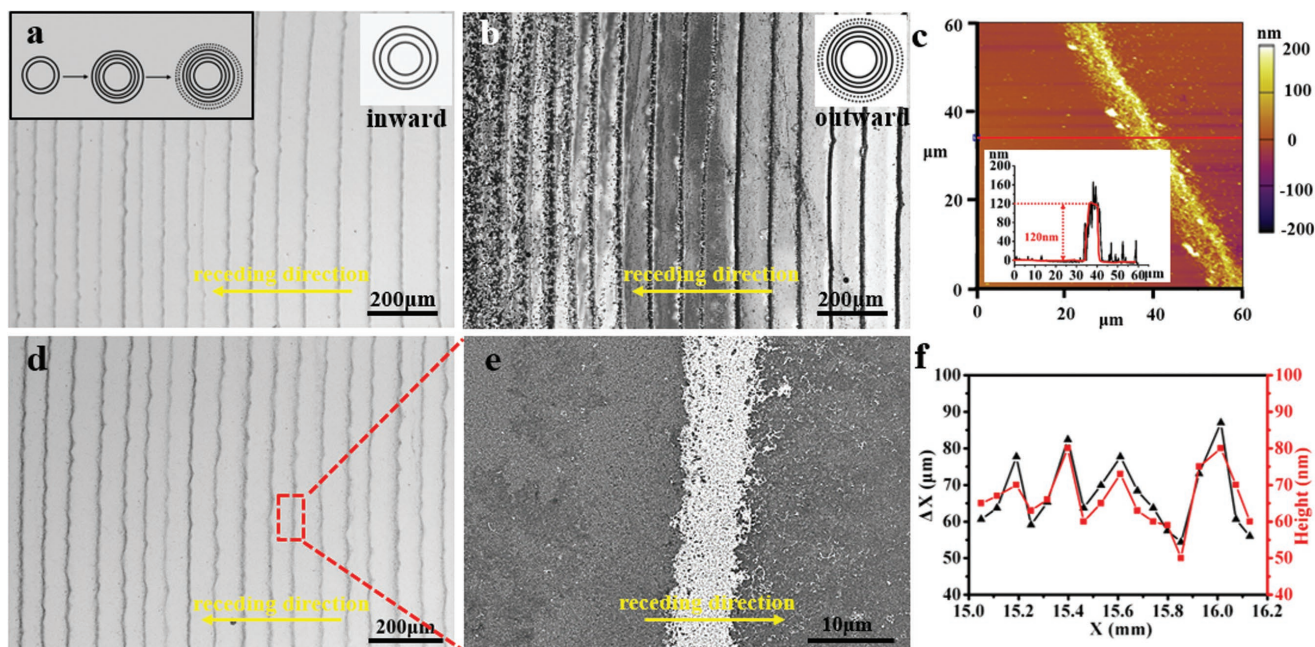

Figure 2. Homocentric MWCNT ring pattern self-assembled on a Si-SiO$_2$ substrate. a,b) Optical images of closely and scatteredly packed MWCNT rings on the inside (a) and outside (b) position on the Si-SiO$_2$ substrate. c) AFM image of a single closely packed MWCNT ring. d) Optical image of closely packed MWCNT rings with various intervals (i.e., ΔX, as defined in Figure 4f). f) Seventeen heights and intervals of the rings from right to left in (d) are plotted. e) SEM image of a single closely stacked MWCNT ring with a neat edge. The yellow arrows represent the CL receding direction.

Table 1. Hamaker constants of different materials.[6]

Materials	SiO$_2$[6a]	Au[6b]	MWCNTs[6c]
Hamaker constant	6.5×10^{-20}J	45.3×10^{-20}J	6×10^{-19}J

was defined as the height of the MWCNT ring (see inset in Figure 2c). As shown in Figure 2d, closely packed rings with fluctuating intervals were selected to measure the heights and intervals variation with the radial distance of the ring from the cavity center (i.e., X, defined in Figure 4f). Seventeen heights of rings and seventeen intervals of adjacent rings from right to left were measured and are plotted in Figure 2f. The heights and intervals had a similar variation trend with X. (MWCNT rings with well controlled placements and periodicity are shown in Figure S1 and S2 in the Supporting Information.)

Various environmental factors (e.g., chemical modification, temperature, humidity, pressure), and the van der Waals (VDW) force, governed by the Hamaker constant, play a vital role in the self-assembly process of nonvolatile solutes.[5–7] As a metallic material, Au has a much higher Hamaker constant than SiO$_2$ (**Table 1**), which means a much higher VDW force to pin MWCNT bundles on the Au substrate.[6b] To explore the influence of the VDW force on the shape of the MWCNT rings, we selected a Au thin film as another substrate for MWNCT self-assembly.

Interestingly, on the Au substrate, smoothly packed MWCNT rings, rings with waviness, and rings with shuttle-like holes formed from the inside to the outside successively (see inset in **Figure 3**a). Smoothly packed MWCNT rings with fluctuating intervals in the inside position were selected

for measuring the intervals and heights (see Figure 3a). The MWCNTs in the smoothly packed ring showed a hierarchical distribution along the receding direction of the CL (see Figure 3b). Depending on their dimensional difference, the MWCNTs could be divided into three continuous sections (I, II, and III) along the receding direction. Part I mainly consisted of MWCNT bundles with a short average length and radius. Part II mainly consisted of MWCNT bundles with a long average length and radius. Part III consisted of hybrid-sized MWCNTs bundles. This specific distribution of vari-sized MWCNTs on smooth rings provided a new method to verify the dimensional homogeneity of MWCNTs at the nanoscale.

The height of a single MWCNT ring on a Au substrate is shown in Figure 3c. The smooth MWCNT ring showed a flocculent edge (I and III) and possessed an arched height profile (see fitted red curve). The distance between the top and bottom of the arch was defined as the height of the MWCNT ring (see inset in Figure 3c).

As shown in Figure 3d, smooth rings, rings with waviness, and shuttle-like holes were formed successively along the receding direction on the outside. Shuttle-like holes with junctions formed between the adjacent MWCNT rings in the outermost position of the cavity. Some sporadic MWCNT bundles existed in the shuttle-like holes (see Figure 3e). Twelve heights and intervals of adjacent rings from right to left in Figure 3a were measured and are plotted in Figure 3f. The heights and intervals had a similar variation trend with X, see comparison of Figure 3f and Figure 2f. This implies that the self-assembled higher rings tend to induce a greater recession of CL and formed a wider interval to begin the next self-assembly process (explanation see further).
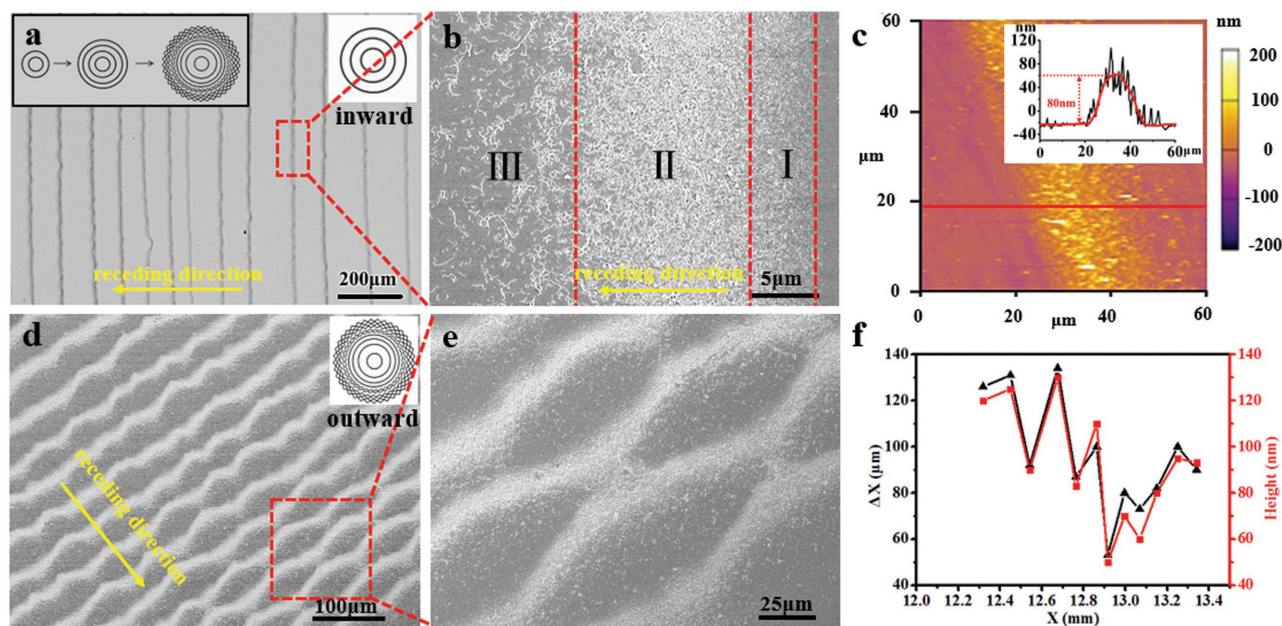

Figure 3. Homocentric MWCNT ring pattern formation on a Au substrate. a) Optical images of smooth rings formed on the inside. b) SEM image of a single smooth ring. The ring was divided into three parts (I, II, and III) based on the distribution difference of the MWCNTs. c) AFM image of a single smooth ring. d) SEM image of smooth MWCNT rings, rings with waviness, and rings with shuttle-like holes. e) Enlarged SEM image of shuttle-like holes. The yellow arrows represent the CL receding direction. f) Twelve heights and intervals of rings from right to left in (a) are plotted.

Dynamic Mechanism Analysis of MWCNT Self-Assembly: Based on the experimental results and real-time videos, a simulation model was built to explore the characteristics and causes of the shapes of the MWCNT rings on Si-SiO$_2$ and Au substrates. As shown in **Figure 4**a, the MWCNT dispersion solution formed a circular opening in the cavity center. Single MWCNTs (Figure S3, Supporting Information) aggregated into MWCNT bundles (small blue particles) (Figure S4, Supporting Information) because of the evaporation of the DI water. The MWCNT bundles were transmitted from the outside to the inside by convection flow (Figure 4b and Video 1, Supporting Information). Parts of the MWCNT bundles were pinned on the substrate surface under the action of a larger pinning force (red arrow in Figure 4d). The rest swirled away from the CL and back to the inner solution under the combined action of surface tension and larger capillary force (green arrow in Figure 4d). The pinning force mainly originated from VDW forces and surface roughness.[7e] The pinned MWCNT bundles created a local surface roughness, which in turn pinned the CL for further self-assembly of MWCNTs into a ring. The returned MWCNT bundles continued to aggregate with later formed MWCNT individuals or bundles into bulky aggregated MWCNT particles (large blue particle). The MWCNT bundles with a short average length and radius self-assembled into closely packed rings

and smoothly packed rings on the inside at the early stage on the Si-SiO$_2$ and Au substrates, respectively (Figure 2a and Figure 3a). A higher proportion of bulky aggregated MWCNT particles and a lower proportion of MWCNT bundles self-assembled into scattered packed rings on the outside at a later stage on the Si-SiO$_2$ substrate (Figure 2b). A higher proportion of MWCNT bundles and lower proportion of bulky aggregated MWCNT particles self-assembled into wave-like rings and rings with shuttle-like holes on the outside at a later stage on the Au substrate.

As shown in Figure 4c, the initial liquid level H achieved an initial contact angle θ_0 when the MWCNT dispersion solution achieved a hydrodynamic equilibrium. Due to evaporation θ_0 decreased gradually to a critical contact angle θ_i (Figure 4e and f) at which the surface tension exceeded the pinning force.[7e,8] This results in the recession of CL to a new position for the next self-assembly process by a zipper-like movement (**Figure 5** and Video 2, Supporting Information). Smooth and failed recession resulted in smooth rings and junctions between adjacent rings, respectively (Video 3 and 4, Supporting Information). Additionally, vari-sized impurities also had a significant influence on the ring structures (Figure S5 and Video 5, Supporting Information). Without taking into account the loss of DI water during the rapid recession of the CL to a new position, the evaporated mass
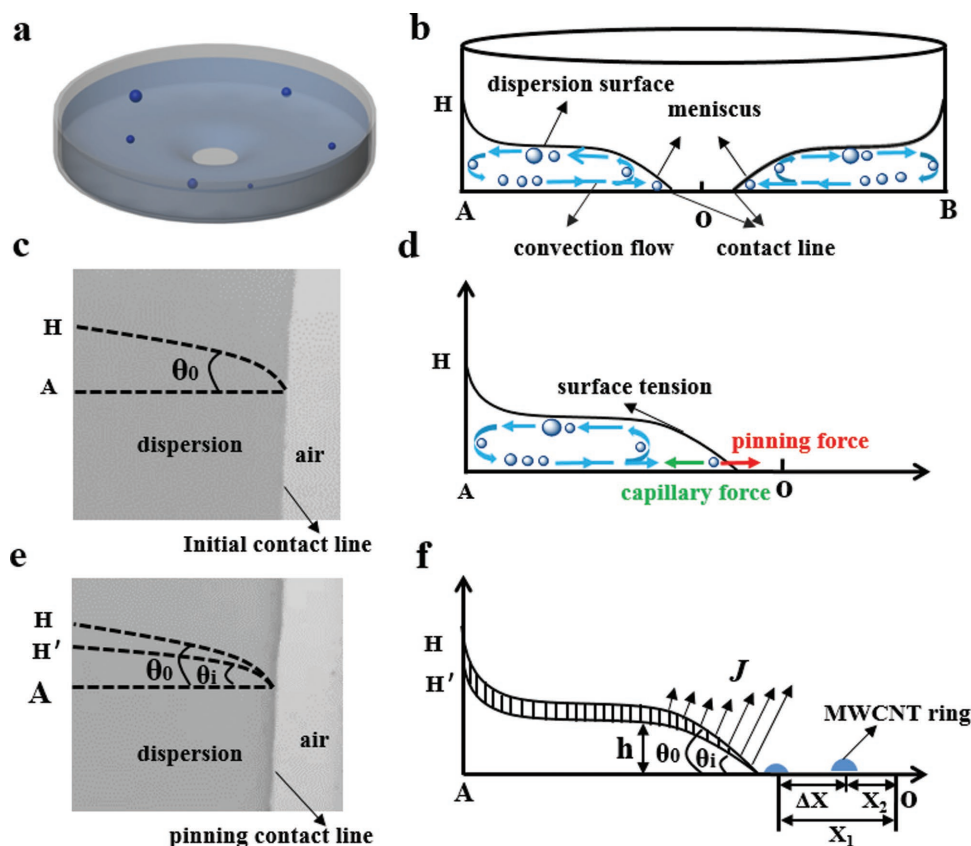

Figure 4. Mechanism of homocentric MWCNT rings self-assembly on Si-SiO$_2$ and Au substrates. a) 3D view of MWCNT dispersion solution with a circular opening. b) Cross-sectional view of dynamic movement of large MWCNT bundles and bulky aggregated MWCNT particles. c,e) Optical images of initial and pinning CL, respectively. d,f) Cross-section view correlated to (c,e), respectively. H and H' represent the liquid surface before and after DI water evaporation. A and h represent the substrate surface and meniscus height, respectively. X represents the distance of the MWCNT rings from the cavity center. $\Delta X = X_1 - X_2$.
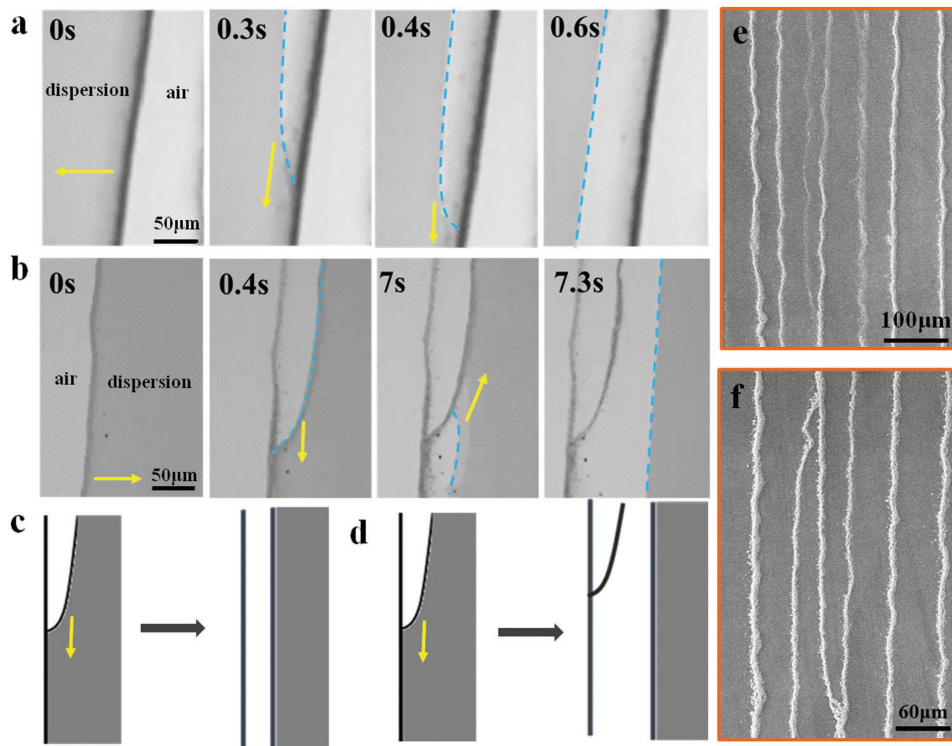
Figure 5. Zipper-like movement of the CL along preformed MWCNT rings. a,b) Optical images of smooth recession and failed recession of CL on a Si-SiO$_2$ and a Au substrate, respectively. c,d) Simulation diagrams of smooth recession and failed recession of CL, respectively. e,f) SEM images of junctions formed between adjacent rings because of failed recession of CL for one and two times on a Si-SiO$_2$ substrate. The yellow arrows represent the receding direction of the CL. The blue curves represent the zipper-like movement of the CL.

flux per unit area unit time (J)[2] (vertically striped region in Figure 4f) can be given by

$$J \propto \Delta X^{-(\pi-2\theta)/(2\pi-2\theta)} \tag{1}$$

where ΔX is the interval between any two adjacent rings, and θ is the contact angle. A higher height of a single ring results in a decrease in the critical contact angle θ_i.[7e,f,8d,e] A smaller θ_i implies a longer pinning time for self-assembly, which in turn leads to a greater volume loss (i.e., ΔV) removed by J. As a result, it leads to a larger recession (i.e., ΔX) of CL to reach the initial contact angle θ_0.[8] This theory is in accordance with the heights and intervals variation trends shown in Figure 2f and Figure 3f.

Comparing Figure 2e with Figure 3b, the distribution difference of the MWCNTs on both substrates can be attributed to the difference in VDW interaction potential and VDW forces,[9] which can be given by

$$E_{\text{VDW}} = -\frac{H_{12}L\sqrt{R}}{12\sqrt{2}D^{3/2}} \tag{2}$$

$$F_{\text{VDW}} = -\frac{H_{12}L\sqrt{R}}{8\sqrt{2}D^{5/2}} \tag{3}$$

where E_{VDW} and F_{VDW} represent the VDW interaction potential and VDW force, respectively. E_{VDW} and F_{VDW} can be used to estimate the binding energy and adhesion force between the nonvolatile solutes and the substrate surface. E_{VDW} and F_{VDW} imply the difficulty of adhesion of the nonvolatile

solute on the substrate. H_{12} is the equivalent Hamaker constant of two different interactional materials; L is the average length of the MWCNT bundles; R is the average radius of the MWCNT bundles ($R > D$); D is the distance between two interacting surfaces. A negative F_{VDW} implies an attraction (H_{12} positive), whereas a positive F_{VDW} implies a repulsion (H_{12} negative). For MWCNT bundles with the same L and R, it is so that the smaller D was, the stronger the adhesion achieved between the MWCNT bundle and the substrate. For the same D, the larger R was, the larger the adhesion per unit length achieved between the MWCNT bundle and the substrate. For the same D and R, the larger L was, the larger the adhesion achieved between the MWCNT bundles and the substrate. Here, H_{12} can be given by[10]

$$H_{12} = \sqrt{H_1 H_2} \tag{4}$$

where H_1 and H_2 are the Hamaker constants for the individual interactional materials. The Hamaker constants of the different materials are shown in Table 1. Based on Equations (2), (3), and (4), we can obtain the following simplified expression (see detailed derivation process in the Supporting Information) for same-sized MWCNT bundles

$$\frac{E_{\text{Au-(MWCNT-SDBS)}}}{E_{\text{SiO2-(MWCNT-SDBS)}}} = \frac{F_{\text{Au-(MWCNT-SDBS)}}}{F_{\text{SiO2-(MWCNT-SDBS)}}}$$

$$= \frac{H_{\text{Au-(MWCNT-SDBS)}}}{H_{\text{SiO2-(MWCNT-SDBS)}}} = \frac{\sqrt{H_{\text{Au}}}}{\sqrt{H_{\text{SiO2}}}} \approx 2.64 \tag{5}$$

where "MWCNT-SDBS" represents MWCNTs covered with sodium dodecyl benzene sulfonate (SDBS). The larger $E_{\text{Au-(MWCNT-SDBS)}}$ and $F_{\text{Au-(MWCNT-SDBS)}}$ indicate that MWCNTs adhesion occurred more easily and tightly on the Au substrate. A larger $E_{\text{Au-(MWCNT-SDBS)}}$ and $F_{\text{Au-(MWCNT-SDBS)}}$ lead to the pinning of the MWCNT bundles with small average length and radius on the Au substrate, which formed part I in Figure 3b. A larger $E_{\text{Au-(MWCNT-SDBS)}}$ and $F_{\text{Au-(MWCNT-SDBS)}}$ also contributed to the pinning of MWCNT bundles from the rapid zipper-like recession of CL, which resulted in MWCNT bundles self-assembling into part III in Figure 3b.

The $E_{\text{SiO2-(MWCNT-SDBS)}}$ and $F_{\text{SiO2-(MWCNT-SDBS)}}$ are much smaller than $E_{\text{Au-(MWCNT-SDBS)}}$ and $F_{\text{Au-(MWCNT-SDBS)}}$. Therefore, few MWCNT bundles were pinned down on the silicon wafer substrate from the rapid zipper-like recession of CL, which resulted in the neat edge of the MWCNT rings (Figure 2e). Meanwhile, parts of the MWCNT bundles with small average length and radius swirled back to the inner solution and continued to aggregate with later formed MWCNT bundles, forming large MWCNT bundles and bulky aggregated MWCNT particles on the Si-SiO$_2$ substrate. These large MWCNT bundles and bulky aggregated MWCNT particles self-assembled into closely packed and scattered packed rings from the inside to the outside on the Si-SiO$_2$ substrate, respectively (Figure 2b and Figure S6, Supporting Information).

Receding Mode of CL Along MWCNT Rings on Si-SiO$_2$ Substrate and Smooth MWCNT Rings on Au Substrate: The MWCNT rings were always accompanied by a dynamic zipper-like propagation along the closely packed and scattered packed MWCNT rings on the Si-SiO$_2$ substrate and smooth rings on the Au substrate, respectively (see Figure 5a and b). The zipper-like CL (blue curve) originated from outside of the field of view and propagated forward along the pre-existing MWCNT deposition. The entire recession process took about 0.6 s, which was timed with a stopwatch, which indicates a more rapid velocity than previously reported.[11] Furthermore, the majority of intervals between adjacent rings are also larger than previously reported for parallel stripes.[3a,11] We attributed these features to the high evaporation temperature, which offered a larger migration driving force and evaporation rate.

External interference or local impurities tend to induce failing separation. This failing separation may cause one or more junctions between adjacent MWCNT rings. As shown in Figure 5b, the zipper-like CL suspended for about 6.6 s (0.4 s–7 s, see Video 3 at 00:00:06 – 00:00:13) until a new zipper-like propagation (see Video 3 at 00:00:14) broke the equilibrium and the recession continued smoothly. Both of the movement types can be summarized in a simple schematic diagram (Figure 5c and d). Local parallel rings (Figure 5c) and cross-linked junctions (Figure 5d) were formed from the smooth separation and failed separation of the CL, respectively. As shown in Figure 5e and f, one and two cross-linked junctions formed on the Si-SiO$_2$ substrate because of failed separation. The failed separation also extended the self-assembly time and contributed to the closely stacked structure formation (Video 3 and 4, Supporting Information).

Receding Mode and Mechanism Analysis of Wave-like CL and Wave-like MWCNT Rings on Au Substrate: To analyze the receding modes and mechanism of wave-like CL and MWNCT rings on the Au substrate, we investigated the pattern transition of the MWCNT rings from the inside to the outside on both Si-SiO$_2$ and Au substrates. As shown in **Figure 6**a and b, closely packed and scattered packed rings formed on the inside and outside, respectively, on the Si-SiO$_2$ substrate. Seventeen intervals of adjacent rings from right to left in Figure 6a were measured and are plotted in Figure 6c. The intervals show a decreasing trend with radial distance X from the inside to the outside. As shown in Figure 6d and e, smoothly packed rings and rings with waviness formed on the inside and outside, respectively, on the Au substrate. Eighteen intervals of adjacent rings from right to left in Figure 6d were measured and are plotted in Figure 6f. The intervals of Figure 6f show a similar decreasing trend than those in Figure 6c. As a whole, hundreds of rings on both substrates showed a decreasing trend. This gradient feature can be attributed to the imbalance between the linear pinning force and the nonlinear capillary force,[8b] which leads to a nonlinear evaporated DI water volume (ΔV). Finally, the nonlinear ΔV leads to a gradient decreasing trend of ΔX with X.

Flow instability[12] can induce kinks, which are distributed randomly along a single MWCNT ring at the early stage. As shown in Figure 6e and Figure 3d, the kinks in the MWCNT rings increased along the receding direction of the CL. The larger F_{VDW} between the MWCNT bundles and the Au substrate contribute to the retention and reproduction of kinks. These kinks acted as the origin of waviness and propagated along the receding direction. The later ring retained the tortuous shape of the front ring and reproduced new kinks along the receding direction. Finally, randomly distributed kinks gradually transitioned into waviness and shuttle-like holes from the inside to the outside. The dispersion relation that quantifies kinks can be given by[13]

$$\Omega = -q^4 + \frac{H_{12}}{2\pi h^4 \gamma}q^2 \tag{6}$$

$$q = \frac{1}{2h^2} \times \sqrt{H_{12}/\pi\gamma} \tag{7}$$

where Ω is the growth rate of the kinks; q is the growth mode; γ is the surface tension of the MWCNT dispersion solution; and h is the height of the meniscus. According to Equations (4), (6), and (7), the MWCNT bundles with a larger $H_{\text{Au-MWCNT}}$ are more conducive to induce kinks, which is in accordance with our experimental results.

As shown in Figure 6g, a wave-like ring was divided by a green vertical central axle into two sides. The left and right sides were defined as the wave crest and trough, respectively. Interestingly, the wave crests always face the wave troughs between two adjacent rings (Figure 3d and Figure 6e). We also recorded the dynamic process of the wave ring self-assembly (Video 6, Supporting Information). As shown in Figure 6h, we simulated the dynamic self-assembly process of wave-like MWCNT rings on a Au substrate. The wave crests were in front of the wave troughs and reached a critical
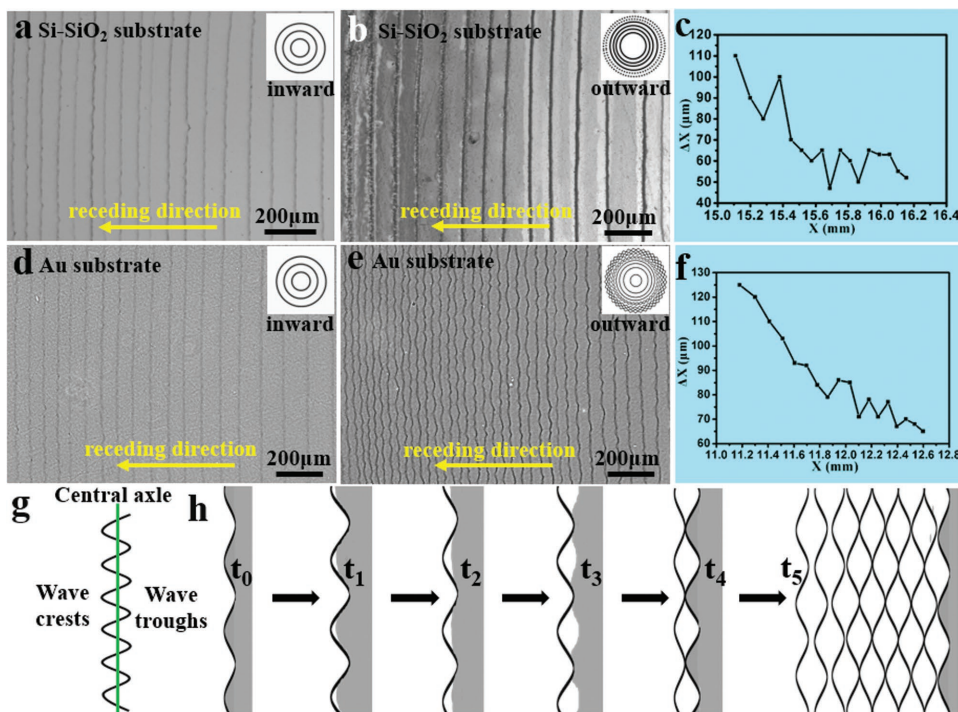
Figure 6. Surface pattern transition of MWCNT rings from the inside position to the outside position on Si-SiO$_2$ and Au substrates. a,b) Optical images of closely packed and scatteredly packed rings, respectively. d,e) Optical images of smoothly packed rings on the inside and rings with waviness on the outside, respectively. The intervals in (a) and (d) are plotted in (c) and (f), respectively. g) Definition of wave crests and troughs by dividing a wavy ring using a green vertical central axle. h) Simulation diagram of progressive formation of wavy rings and rings with shuttle-like holes. The yellow arrows represent the receding direction of the CL.

contact angle in advance (t_0). Therefore, the CL, which was pinned by the wave crests, receded first (t_1). The evenly distributed wave crests acted as the origin of the CL recession and induced a pinning and slipping movement of wavy CL on the Au substrate (Video 6). Because of the difference in surface roughness between the Au substrate and the MWCNT ring this results in different pinning forces in the CL, and the receding velocity of the CL was faster on the Au substrate than on the MWCNT ring (t_2). The difference in receding velocity resulted in the next wave-like CL (t_3). Moreover, the MWCNTs pinned on the Au substrate stabilized the waviness of the CL for further self-assembly of the rings (t_4). Finally, the wave crests and wave troughs in the front MWCNT ring transitioned into wave troughs and wave crests in the next ring (t_5). The repeatability of the wave troughs and wave crests resulted in wave-like rings (Figure 6e). The gradient decrease of ring intervals resulted in the shuttle-like holes (Figure 6e and f).

In summary, a thermo-driven evaporation self-assembly system confined with a hollow cylinder geometry was designed successfully. Differently shaped homocentric MWCNT rings were for the first time directly self-assembled on rigid, flexible, and transparent substrates with different Hamaker constants. Based on the different Hamaker constants, closely packed and scatteredly packed homocentric MWCNT rings were fabricated simultaneously on a Si-SiO$_2$ substrate. Smooth MWCNT rings, rings with waviness, and rings with shuttle-like holes were fabricated simultaneously on a Au substrate. We clearly observed the dynamic

movement trace of bulky aggregated MWCNT particles in the convection flow by optical microscopy. The dynamic movement of MWCNT aggregations included two processes with different directions: i) MWCNT bundles transmitted from the inside to the CL for self-assembly by convection flow; ii) MWCNT bundles returned from the CL to the inner solution for further aggregation by swirling flow. This finding supplemented the mechanisms of self-assembly of nonvolatile solutes. Based on the different Hamaker constants and dynamic movement model, we analyzed the self-assembly mechanism of the homocentric MWCNT rings on both Si-SiO$_2$ and Au substrates. The analysis was in good accordance with our experimental results. The specific distribution of vari-sized MWCNTs in smooth rings provided a new method to verify the dimensional homogeneity of MWCNTs at the nanoscale on a Au substrate. Furthermore, this low-cost, manageable method of MWCNT ring self-assembly opens up new avenues for fabricating harmonic oscillators, tissue engineering scaffolds, and ring-like patterns for flexible transparent applications.

Supporting Information

Supporting Information is available from the Wiley Online Library or from the author.

[1] a) L. Ding, D. Yuan, J. Liu, *J. Am. Chem. Soc.* **2008**, *130*, 5428; b) H. Zeng, K. Kristiansen, P. Wang, J. Bergli, J. Israelachvili, *Langmuir* **2011**, *27*, 7163; c) X. Li, C. Wang, J. Shao, Y. Ding, H. Tian, X. Li, L. Wang, *ACS Appl. Mater. Interfaces* **2014**, *6*, 20300; d) Y. J. Chen, K. Suzuki, H. Mahara, T. Yamaguchi, *Chem. Phys. Lett.* **2012**, *529*, 74; e) B. Li, C. Zhang, B. Jiang, W. Han, Z. Lin, *Angew. Chem. Int. Ed.* **2015**, *54*, 4250.

[2] R. D. Deegan, O. Bakajin, T. F. Dupont, G. Huber, S. R. Nagel, T. A. Witten, *Nature* **1997**, *389*, 827.

[3] a) M. Engel, J. P. Small, M. Steiner, M. Freitag, A. A. Green, M. C. Hersam, P. Avouris, *ACS Nano* **2008**, *2*, 2445; b) R. Martel, *ACS Nano* **2008**, *2*, 2195; c) Z. Zanolli, R. Leghrib, A. Felten, J. J. Pireaux, E. Llobet, J. C. Charlier, *ACS Nano* **2011**, *5*, 4592; d) J. T. Wen, C. M. Ho, P. B. Lillehoj, *Langmuir* **2013**, *29*, 8440; e) X. X. Wang, W. Jiang, Q. Zheng, L. Yan, Y. M. Jin, C. B. Han, J. Zhuang, H. Liu, Z. Li, *Small* **2015**, *37*, 4864.

[4] H. Li, H. Z. Geng, Y. Meng, Y. Wang, X. B. Xu, E. X. Ding, S. Ma, *Appl. Surf. Sci.* **2014**, *313*, 220.

[5] a) S. W. Hong, W. Jeong, H. Ko, M. R. Kessler, V. V. Tsukruk, Z. Lin, *Adv. Funct. Mater.* **2008**, *18*, 2114; b) H. Park, A. Afzali, S. J. Han, G. S. Tulevski, A. D. Franklin, J. Tersoff, W. Haensch, *Nat. Nanotechnol.* **2012**, *7*, 787; c) R. Kumar, C. N. R. Rao, *J. Mater. Chem. A* **2015**, *3*, 6747; d) J. Wu, A. Antaris, M. Gong, H. Dai, *Adv. Mater.* **2014**, *26*, 6151; e) Y. Joo, G. J. Brady, M. S. Arnold, P. Gopalan, *Langmuir* **2014**, *30*, 3460.

[6] a) T. J. Senden, C. J. Drummond, *Colloids Surf. A* **1995**, *94*, 29; b) E. M. Hotze, T. Phenrat, G. V. Lowry, *J. Environ. Qual.* **2010**, *39*, 1909; c) H. Somada, K. Hirahara, S. Akita, *Nano Lett.* **2009**, *9*, 62.

[7] a) M. Maillard, L. Motte, M. P. Pileni, *Adv. Mater.* **2001**, *13*, 200; b) A. V. Lyushnin, A. A. Golovin, L. M. Pismen, *Phys. Rev. E* **2002**, *65*, 1; c) A. Askounis, K. Sefiane, V. Koutsos, M. E. Shanahan, *Colloids Surf. A: Physicochem. Eng. Aspects* **2014**, *441*, 855; d) M. D. Morariu, E. Schäffer, U. Steiner, *Eur. Phys. J.* **2003**, *12*, 375; e) R. D. Deegan, O. Bakajin, T. F. Dupont, G. Huber, S. R. Nagel, T. A. Witten, *Phys. Rev. E* **2000**, *62*, 756; f) P. G. De Gennes, *Rev. Mod. Phys.* **1985**, *57*, 827.

[8] a) R. D. Deegan, *Phys. Rev. E* **2000**, *61*, 475; b) J. Xu, J. Xia, S. W. Hong, Z. Lin, F. Qiu, Y. Yang, *Phys. Rev. Lett.* **2006**, *96*, 066104; c) Y. O. Popov, *Phys. Rev. E* **2005**, *71*, 036313; d) B. J. Fischer, *Langmuir* **2002**, *18*, 60; e) Y. O. Popov, T. A. Witten, *Phys. Rev. E* **2003**, *68*, 036306.

[9] a) D. Leckband, J. Israelachvili, *Q. Rev. Biophys.* **2001**, *34*, 105; b) M. F. Yu, T. Kowalewski, R. S. Ruoff, *Phys. Rev. Lett.* **2001**, *86*, 87.

[10] M. Götzinger, W. Peukert, *Langmuir* **2004**, *20*, 5298.

[11] H. Li, T. C. Hain, A. Muzha, F. Schöppler, T. Hertel, *ACS Nano* **2014**, *8*, 6417.

[12] S. Lin-Gibson, J. A. Pathak, E. A. Grulke, H. Wang, E. K. Hobbie, *Phys. Rev. Lett.* **2004**, *92*, 048302.

[13] a) A. Sharma, *Langmuir* **1993**, *9*, 861; b) I. Leizerson, S. G. Lipson, A. V. Lyushnin, *Langmuir* **2004**, *20*, 291.